Manufacturing Rev. **12**, 22 (2025)

https://doi.org/10.1051/mfreview/2025017

Manufacturing Review
Available online at:
https://mfr.edp-open.org

ORIGINAL ARTICLE OPEN ACCESS

Investigation of planar anisotropy evolution in aluminium alloy sheets under hot stamping conditions using digital image correlation

Xi Wang[1,2], Ruiqiang Zhang[2,3,*], Zhusheng Shi[2], and Jianguo Lin[2,3]

[1] Department of Mechanical Engineering, University of Science and Technology Beijing, Beijing, PR China
[2] Department of Mechanical Engineering, Imperial College London, London SW7 2AZ, UK
[3] Department of Industrial and Systems Engineering, The Hong Kong Polytechnic University, Hong Kong, PR China

Received: 29 June 2025 / Accepted: 3 September 2025

Abstract. Hot stamping of aluminium alloy sheets is widely used for manufacturing high performance panel components across various industries. However, the anisotropic characteristics of the alloy and their evolution during deformation under hot stamping conditions, remain poorly understood, resulting in significant challenges in accurately determining its thermomechanical behaviour and developing predictive models. To address this knowledge gap, a series of uniaxial tensile tests on a 1.5 mm thick AA6082 sheet under hot deformation conditions were conducted in this study using a Gleeble simulator at temperatures ranging from 350 °C to 500 °C and strain rates of 0.1 s^{-1} and 0.5 s^{-1}. The planar anisotropy along both the length and width directions of AA6082 samples, as well as their evolution during hot deformation was investigated by calculating the r-value (known as the Lankford coefficient) based on the full-field strain distribution within the gauge length, measured using digital image correlation (DIC). The effects of strain fields selected from different regions within the gauge area on the calculated r-value were analysed. An empirical equation for r-value was proposed, for the first time, to model the planar anisotropy evolution across various deformation temperatures and strain rates under hot stamping conditions. This equation was subsequently applied to correct the stress-strain curves obtained using the C-gauge, an alternative strain measurement method, and the corrected data were compared with curves measured by DIC. This study provides insights on accurately determining thermomechanical behaviour and developing predictive models of aluminium alloys under hot stamping conditions.

Keywords: Planar anisotropy / aluminium alloy / hot stamping / digital image correlation / Lankford coefficient

1 Introduction

The demand of employing high strength, lightweight aluminium alloy components in vehicle manufacturing and aerospace industry has been continuously increasing in recent years [1,2]. Advanced manufacturing techniques such as hot stamping and extrusion have been developed for fabricating thin-walled sheet components with complex shapes [3–5]. In these forming processes, the alloy is heated to a certain temperature and then deformed in specific tools to achieve the designed shape with improved formability at the high forming temperature. To capture the alloy's deformation behaviour in the deformation processes with corresponding temperature profile, the Gleeble thermal-mechanical simulator has been extensively employed due to its ability to precisely control both the testing temperature and strain rate over a wide range [6–8]. Li et al. [9] investigated the thermomechanical behaviour of boron steel in hot stamping by employing the Gleeble to perform high temperature tensile tests ranging from 20 to 900 °C, with the strain rate from 0.01 to 10 s^{-1}. Zhang et al. [10] performed the tensile tests in Gleeble simulator at temperatures of 375 and 450 °C with strain rates of 0.1 to 0.5 s^{-1} to capture the thermomechanical behaviours of AA6082 in hot stamping. The key reason for obtaining stress-strain relationships across a wide range of deformation temperatures and strain rates is to provide essential data for constitutive and process modelling of the material in hot stamping. These data provide the foundation for ensuring the feasibility and accuracy of predicting material behaviour during the fabrication processes [9,11].

In the Gleeble tensile test system, in addition to controlling deformation temperatures and strain rates, accurate strain measurement technique is crucial for properly depicting the stress-strain relationship during the deformation process [12,13]. Multiple methods have been adopted in measuring the strain of the specimens

* e-mail: r.zhang17@imperial.ac.uk

during Gleeble tensile tests, such as relying on recording the displacements of the jaws/grips [14,15], placing strain gauge rosettes on the specimen surface [16], employing C-gauges to measure the diametric or width change of the specimen during deformation [17,18], and directly placing L-gauges along the length of the specimen to obtain strain data [12,19]. Although the Gleeble simulator can produce variable deformation temperatures and strain rates to capture the material's deformation behaviour in hot stamping process, one limitation still exists is that the temperature gradient along the specimen length direction caused by the heat loss to specimen grips can affect the characterisation of thermomechanical properties of the material [10,20]. For instance, the fracture strain and tensile strength of boron steel at the temperature of 700 °C and strain rate of 0.1 s^{-1} show significant variation depending on the gauge lengths used from 15 to 30 mm, with the determined fracture strain ranging from 13% to 53% and strength between 213 and 260 MPa [9,21,22]. The inconsistency in tensile tests with varying gauge lengths can result in substantial effects on the determination of constitutive relations and the subsequent prediction of material behaviour. Therefore, it is of significance to obtain an in-depth understanding of the strain evolutions across the full field and their influence on the determination of the stress-strain results during deformation.

More recently, increasing investigations have adopted the non-contact strain measurement method known as digital image correlation (DIC) in the Gleeble tensile tests [23,24]. By painting high contrast random speckle patterns on the surface of the specimen's gauge area, this method offers advantages in depicting a comprehensive strain field of the specimen during large deformation [10]. Shao et al. [25] utilised a paint consisting of amorphous precipitated silica and titanium dioxide for high temperature strain measurements, which can withstand temperatures up to 1093 °C to generate the speckle patterns. The strain fields of AA6082 deformed at temperature between 400 and 500 °C and strain rates from 0.1 to 4 s^{-1} were successfully captured within the small deformation range [25]. However, at high deformation conditions, the shiny effect caused by high temperatures and large deformations degrades the quality of captured deformation images and corresponding failures in the DIC analysis, leading to failures of strain measurements. To overcome this gap, Chen et al. [26] developed a novel procedure for generating more effective speckle patterns utilising a cross-polarisation optical system. The developed system helped to extend the measurable time in the uniaxial and biaxial tests conducted in the Gleeble simulator, allowing for more accurate determination of the thermomechanical properties [26]. By employing DIC measurement, Zhang et al. [27] investigated the strain distribution along the gauge length during deformation of boron steel. Several different gauge lengths were used to evaluate the ductility of the material and found that the determined ductility is highly dependent on the selected gauge length within the strain field measured by DIC. Despite the progress in employing the DIC method to depict a more comprehensive strain filed for the Gleeble tensile tests at high temperatures and deformation rates, the strain distribution and evolution pattern during the test across the full field, along with their effects on the determination of thermal mechanical property as well as anisotropy evolution, still urgently need further exploration.

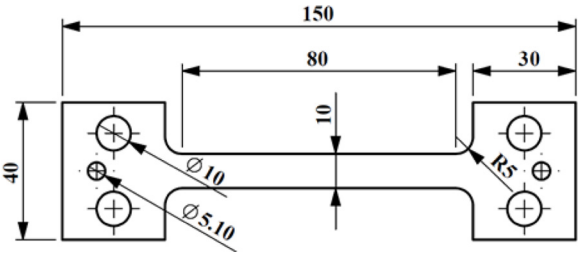

Fig. 1. Specimen geometry and dimensions for Gleeble tensile tests (the unit of dimensions in the figure is mm).

Considering the significance of understanding the full field strain distribution and anisotropy evolution in determining the mechanical properties of the material, it is of substantial urgency to conduct further investigations to resolve this ambiguity. This study aims to explore the characteristics of strain distribution and anisotropy along length and width directions across various selected strain fields in Gleeble tests, as well as providing insights into the evolution of strain distribution and anisotropy with the proceeding of deformation and their effects on the determination of the mechanical properties. In this study, uniaxial tensile tests for AA6082 were conducted using the Gleeble simulator at temperatures ranging from 350 to 500 °C and strain rates of 0.1 and 0.5 s^{-1}. The strain was measured using DIC method and the characteristics of the full filed strain distribution as well as its evolution during deformation was investigated. This study makes its novel contributions in the following aspects: 1) The anisotropy along the length and width directions, and its evolution during deformation under different temperatures and strain rates were studied. 2) A novel empirical relation was proposed to capture the r-value evolution with increasing strain at varying temperatures and strain rates. 3) The stress-strain relations determined using the C-gauge, the DIC method, and the corrected relation based on the established r-value equation were compared and analysed, providing insights on determining the material thermomechanical properties in Gleeble tests using C-gauge and DIC strain measurements.

2 Material and experimental procedures

The material used in this study is aluminium alloy AA6082 sheets with a composition of Al-0.87Si-0.33Fe-0.026Cu-0.51Mn-0.97Mg-0.044Cr-0.025Zn-0.016Ti (wt%). The 1.5 mm thick sheets were cut along the rolling direction into the dog-bone specimens with design and dimensions shown in Figure 1.

The thermomechanical tests were conducted using a Gleeble 3800 thermal-mechanical simulator system demonstrated in Figure 2. This system utilises electric current for heating the specimens via the direct resistance heating method and high-pressure air for cooling. The temperature control during the tensile test was achieved through a pair

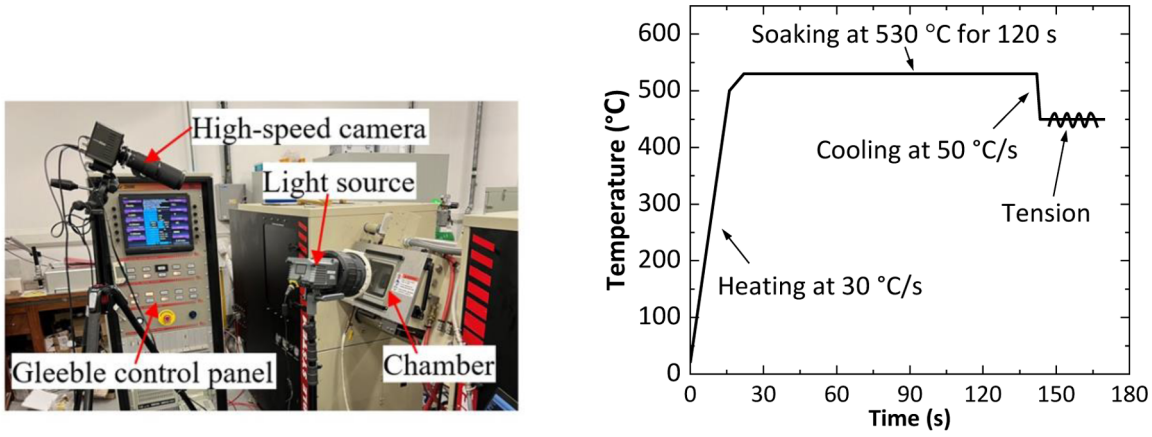

(a) Gleeble and DIC system (b) Thermal profile of AA6082

Fig. 2. Setup for the Gleeble tensile tests and thermal profile for testing AA6082.

Table 1. Test programme for the Gleeble tensile tests of AA6082, including strain measurements using DIC or C-gauge or both.

Test category 1			Test category 2		
Test condition	Temperature	Strain rate	Test condition	Temperature	Strain rate
1A (DIC, C-gauge)	500 °C	0.1 s^{-1}	2A (DIC)	500 °C	0.5 s^{-1}
1B (DIC)	450 °C	0.1 s^{-1}	2B (DIC)	450 °C	0.5 s^{-1}
1C (DIC)	350 °C	0.1 s^{-1}	2C (DIC)	350 °C	0.5 s^{-1}

of *K*-type thermocouples welded at the centre of the specimen. Strain during the tests was measured using a C-gauge extensometer and/or the DIC method. For C-gauge measurements, a C-gauge extensometer with a 12 mm measurement range was positioned parallel to the centre line of the specimen along the width direction to measure changes in width during the tension tests. For DIC measurements, deformation was captured using a high-speed camera Photron FASTCAM Mini UX50 (Photron, Japan) at a resolution of 1280 by 1024 pixels and the cross-polarisation technique [26]. The whole gauge area, where high contrast random speckle patterns were applied, was recorded at a frame rate of 500 frames per second (fps) for strain analysis. The speckle patterns consist of a thin black background layer with random tiny white dots, produced using black and white high-temperature VHT FLAME-PROOF^{TM} paints (Sherwin-Williams, US), respectively [26]. Figure 2b illustrates the thermal profile of the alloy during the tensile test. The specimen was heated to 530 °C for solution heat treatment at an initial heating rate of 30 °C/s which was reduced to 5 °C/s when temperature reaches 500 °C to avoid overheating. After soaking for 120 s, the specimen was quenched at a rate of 50 °C/s to the deformation temperature and held for 2 s to stabilise the temperature. Finally, the specimen was stretched at a specified strain rate. The test conditions including the deformation temperature and strain rate are listed in Table 1.

The deformation images for the tests recorded by the high-speed camera were postprocessed using GOM Correlate 2018, a commercial software package, to establish the full field strains within the gauge area. For the convenience of analysis, the constructed coordinate and selected strain field regions are demonstrated in Figure 3. In this study, as the tensile direction is parallel to the rolling direction of the specimen, the *X*-axis is set parallel to the length of the specimen, while the *Y*-axis is parallel to the width of the specimen. The major true strain is denoted as ε_x to represent the strain along the *X*-axis direction, and the minor true strain is denoted as ε_y as the strain along the *Y*-axis direction. The origin of the coordinate system is located at the centre point as shown in Figure 3b. The total deformation time from the start of the test to specimen failure is defined as t_{tot}, and t represents the deformation time at the current stage. t_n represents the normalised value of the time at current deformation stage expressed as $t_n = t/t_{tot}$, with a value ranging from 0 to 1. Figure 3c demonstrates the temperature distribution along the *X*-axis, obtained from [10] during the Gleeble test under the same conditions. Figure 3d shows the temperature history recorded at different locations along the gauge length during whole deformation at 500 °C and 0.1 s^{-1}. The results indicate that each location remained nearly constant throughout deformation, with variations of less than 2 °C.

To quantitively investigate the evolution of strain and *r*-value across the obtained DIC strain fields, different regions within the specimen gauge area are employed. As exhibited in Figure 3a, the regions are classified into two groups: Group I consists of squares with various sizes including S_1 with a size of 2 mm × 2 mm, S_2 with 4 mm × 4 mm, S_3 with 6 mm × 6 mm, S_4 with 8 mm × 8 mm, while Group II contains regions with the same height and

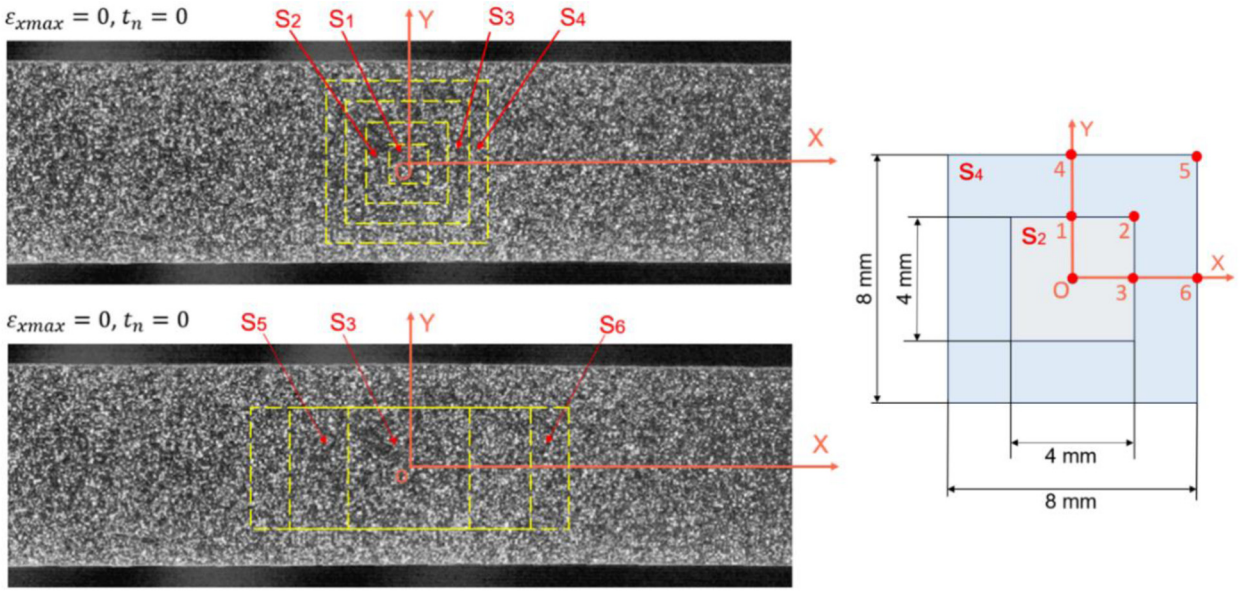

(a) At the beginning $t_n = 0$ of the test with $\varepsilon_{xmax} = 0$

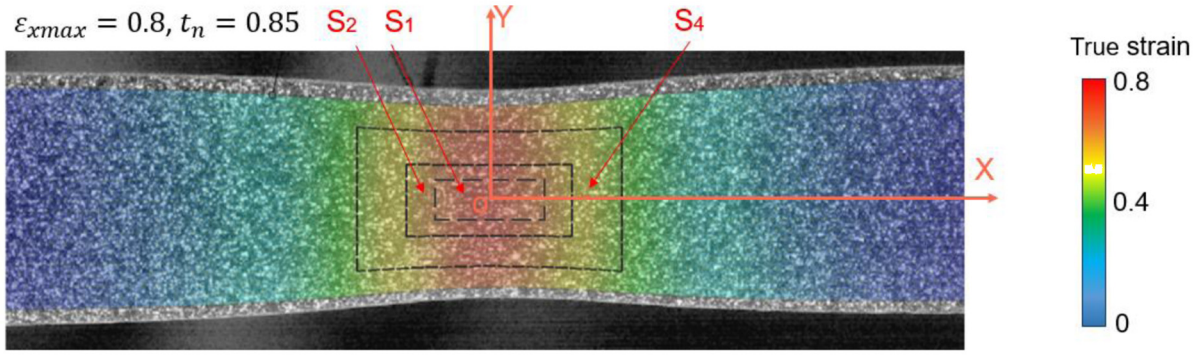

(b) At $t_n = 0.85$ with $\varepsilon_{xmax} = 0.8$

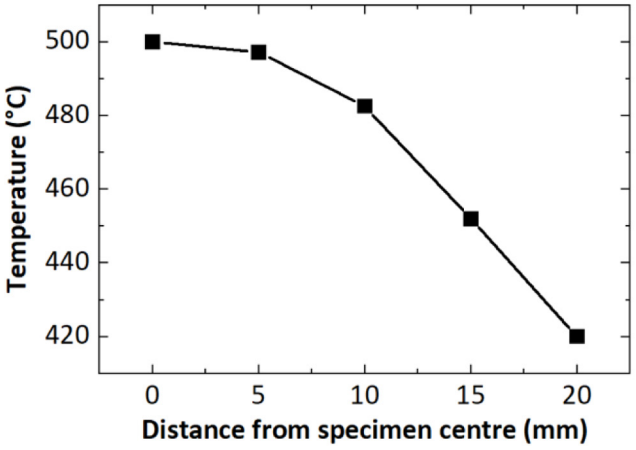

(c) Temperature distribution along the X-axis

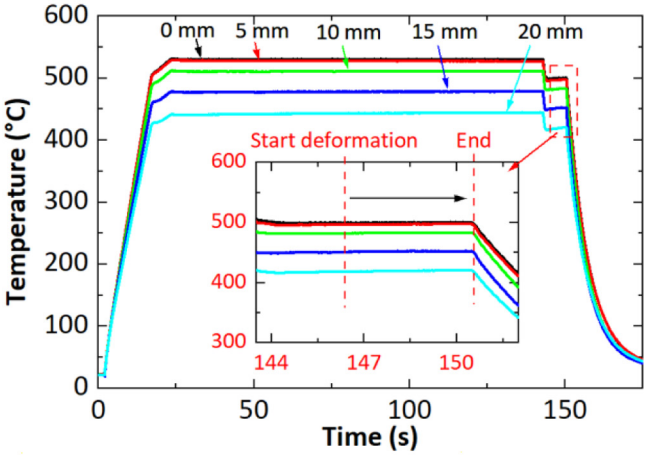

(d) Temperature history during deformation

Fig. 3. Definitions and settings for DIC analysis. ε_{xmax} denotes the highest major true strain along the X-axis direction obtained from the DIC results. The distance in (c) represents the distances of the measured points from point O along the X-axis.

Table 2. Selected regions and their groups.

Group I		Group II	
Region	Size	Region	Size
S_1	2 mm × 2 mm	S_3	6 mm × 6 mm
S_2	4 mm × 4 mm	S_5	6 mm × 12 mm
S_3	6 mm × 6 mm	S_6	6 mm × 18 mm
S_4	8 mm × 8 mm		

different width including S_3 with 6 mm × 6 mm, S_5 with 6 mm × 12 mm and S_6 with 6 mm × 18 mm. The detailed illustration of the region groups is provided in Table 2.

It should be noted that the variation in temperature along *X*-axis is significant, with a drop around 80 °C when the distance is 20 mm away from point O. Therefore, the gauge area from S_1 to S_4 is chosen to investigate the influence of the area on the measured DIC results, as a minor temperature drop of 3 °C is observed within the distance of 5 mm to the point O, as similar to the findings in [28]. On the other hand, when comparing the gauge area of S_3, S_5, and S_6, the temperature variation along the *X*-axis must be considered, as the temperature drops from 500 °C from the centre point O to 483 °C at 10 mm distance away along *X*-axis. Since the temperature distribution in the specimen is not uniform during the test, a reference temperature is adopted in the following context, defined as the temperature measured at the centre point O.

Considering that the specimen's width is 10 mm and temperature variation along the *X*-axis within this range is minor, it can be concluded that temperature distribution along the *Y*-axis of the specimen is more uniform. In addition, it should be noted that the shapes of the regions also change with the ongoing deformation as shown in Figure 3b. The strain and *r*-value evolutions at separate points (O, 1, 2, ..., 6) are studied with their locations demonstrated in Figure 3a. Additionally, the average values of both strain and *r*-value of the regions S_1 to S_6 during deformation process are also investigated.

3 Experimental results

Figure 4 illustrates the evolution of strain and *r*-value for the specimen deformed at the reference temperature 500 °C and strain rate of 0.1 s^{-1} (test condition I). The evolution of the average values of the major and minor strains across the regions S_1 to S_6, as well as the values at the points O to 6 with respect to deformation time are exhibited in Figure. 4a. As seen, the major strain ε_x at all the investigated points increases and the minor strain ε_y decreases as the deformation time progresses. Additionally, points O, 1, and 4, located along the *Y*-axis (centreline of the specimen), exhibit higher absolute strain values (higher major strain and lower minor strain) than other points. In contrast, points 2 and 3, located 2 mm from the *Y*-axis, as well as points 5 and 6, located 4 mm from the *Y*-axis, exhibit lower absolute strain values (lower major strain and higher minor strain), with points 5 and 6 having lower absolute strain values than points 2 and 3.

Figure 4b shows the evolution of average strain within the regions of S_1 to S_6. A similar trend to that observed in Figure 4a can be seen, where major strain values increase and minor strain values decreases with proceeding of deformation. Furthermore, for the regions S_1, S_2, S_3, and S_4, the absolute values of the average major and minor strains decrease with increasing area of the square regions, i.e. the absolute strain values within S_1 to S_4 declines. For region S_3, S_5, and S_6, the average absolute values of the strain decrease with increasing length of the regions from S_3 to S_6.

With the measured major and minor strain, the *r*-value can be calculated using the widely adopted equation:

$$r = \frac{\varepsilon_y}{\varepsilon_z} \tag{1}$$

where ε_y is in-plane strain along the width direction of the specimen (minor strain), ε_z is the out-of-plane strain along the thickness direction of the specimen. By assuming that the specimen remains a constant volume, the equation to calculate the *r*-value can be further expressed as:

$$r = -\frac{\varepsilon_y}{\varepsilon_x + \varepsilon_y} \tag{2}$$

where ε_x denote the major strain. For the isotropic material where $r = 1$ (i.e. $\varepsilon_y = \varepsilon_z$) during deformation, the relationship between ε_x and ε_y can be calculated using equation (2) as $\varepsilon_x = -2\varepsilon_y$. Furthermore, a more divergent *r*-value from 1 indicates higher anisotropy in the deformation along the length and width of the specimen.

Figure 4c demonstrates the evolution of *r*-values for the points of O to 6 as deformation progresses. These *r*-values were calculated using the major and minor strains at the respective locations shown in Figure 4a. Due to small values of ε_y at the beginning of deformation as exhibited in Figure 4a, the *r*-value curves in Figure 4c show fierce fluctuations during the initial stage of deformation. Additionally, the *r*-value curves demonstrate that the points O and 1 to 3, located within the region S_2, have lower *r*-values than the points 4 to 6 located on the edge of region S_4. Points O and 3, located along the *X*-axis, demonstrate lower *r*-values than points 1 and 2, which are positioned 2 mm distance from the *X*-axis. Among points on the edge of region S_4, point 6 (located on the *X*-axis) shows lower *r*-values than points 4 and 5, which are 4 mm from the *X*-axis. These shows that the points located farther from the *X* axis exhibit higher *r*-values.

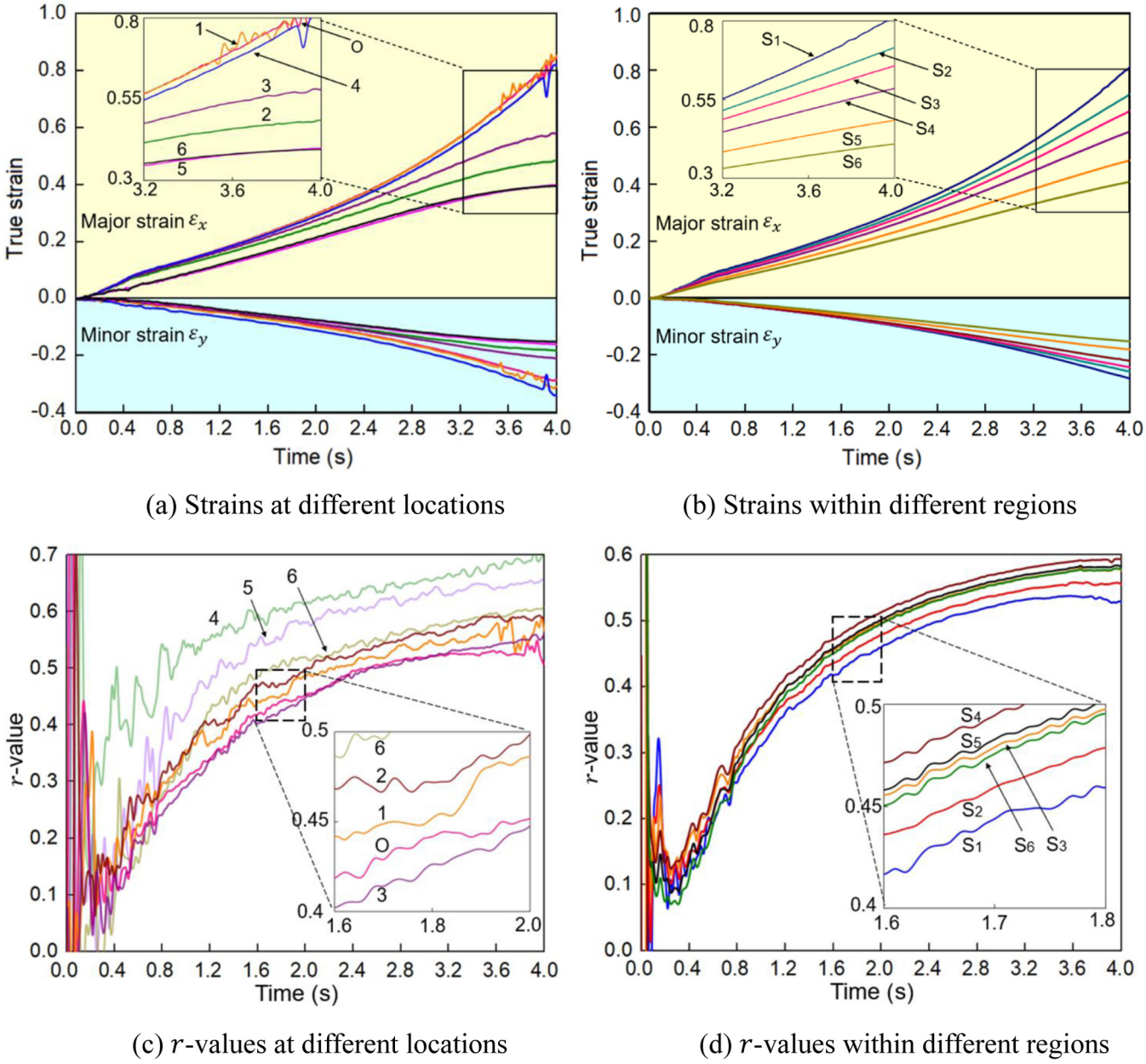

Fig. 4. Variation of the true strains, r-values and strain ratios with proceeding of deformation for specimen tested at the reference temperature of 500 °C and strain rate of 0.1 s^{-1} (test condition 1A as shown in Tab. 1). The locations O to 6 and the regions S_1 to S_6 are shown in Figure 3a.

Figure 4d shows the average r-values within regions from S_1 to S_6. Similar to the r-values demonstrated in Figure 4c, the curves in Figure 4d fluctuate severely at the initial period. Furthermore, the average r-values gradually increase at a decreasing rate. For the Group I regions (S_1 to S_4), the r-value rises with the increase of the region area, i.e. the r-value increases from S_1 to S_4. For the Group II regions (S_3, S_5, and S_6), minor differences are identified for the r-values among these three regions, with S_5 showing the highest value and S_6 the lowest. Overall, the ratio within S_1 has the lowest value and S_4 has the highest.

The average r-value curves within regions S_1 to S_6 demonstrate a similar evolution trend as presented in Figure 4b, where the curves fluctuate at the beginning stage of deformation and gradually increase with the proceeding of deformation until reaching their peak values. This initial severe fluctuation is caused by the experimental errors in the DIC strain measurements: the r-value calculated by equation (2) can vary significantly when considering the measuring error with small values of ε_x and ε_y at the beginning of deformation.

To investigate the strain distribution and its evolution during the deformation process, the major strain ε_x and minor strain ε_y are obtained along the X- and Y-axes, respectively, based on the DIC measurement results. Figure 5 plots the major and minor strain distribution along the X-axis ranging from −5 to 5 mm, and along the Y-axis ranging from −3 and 3 mm at various deformation

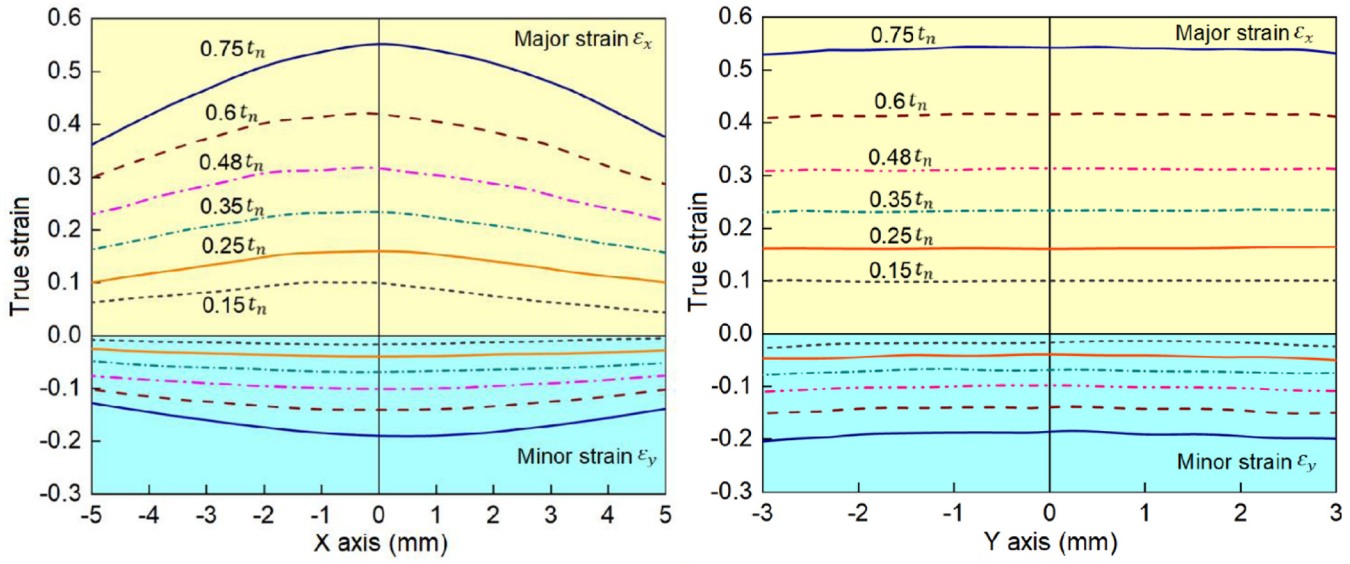

(a) Strain distribution with 500 °C and 0.1 s^{-1} (test condition 1A)

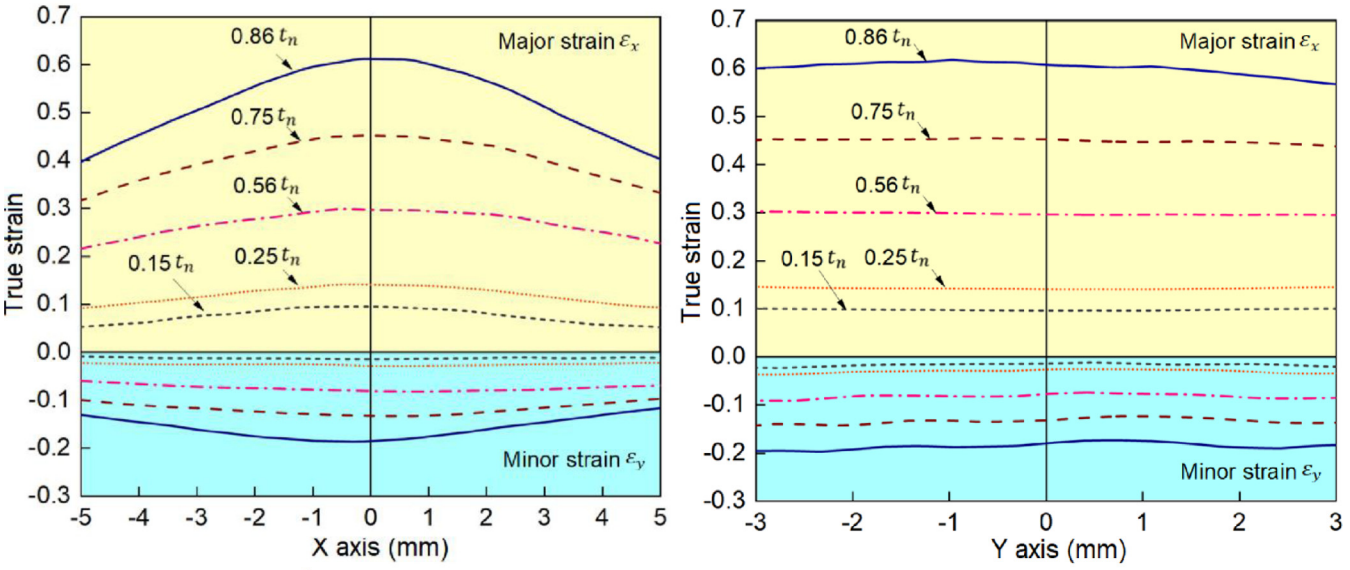

(b) Strain distribution with 350 °C and 0.5 s^{-1} (test condition 2C)

Fig. 5. True major strain and true minor strain distributions at (a) 500 °C and 0.1 s^{-1} (test condition 1A) and (b) 350 °C and 0.5 s^{-1} (test condition 2C) along the X and Y axes at normalised times.

stages. It can be observed that when deformed at various normalised times, for both test conditions 1A and 2C, the divergence in the value of the major strain along the *X*-axis is larger than the corresponding minor strain along the *X*-axis. However, for the major and minor strains along the *Y*-axis, no distinct difference in divergence is observed as the strains along the *Y*-axis remain stable along the deformation process for both specimens.

The DIC method is able to capture the full field strain distribution and its evolution throughout the Gleeble tensile test as demonstrated in Figures 4 and 5. By comparing the strain at different locations illustrated in Figure 4b and the strain distribution and its evolution when deformed at different conditions as shown in Figure 5, a general distribution trend can be observed: the strain significantly decreases along the length direction (*X*-axis) as the distance from the centre point increases, while showing minor fluctuations across the width direction (*Y*-axis).

Figure 6 shows the *r*-value results along the *X*-axis ranging from −5 to 5 mm and along the *Y*-axis ranging from −3 to 3 mm for test conditions 1A and 2C with increasing t_n. The *r*-value was calculated using equation (2), with the obtained major and minor strain distributions along the *X*- and *Y*-axes as shown in Figure 5. It can be observed that the *r*-values on *X*- and *Y*-axes increase with increasing t_n for both specimens. It should be noted that the *r*-value distributions along the *X*- and *Y*-axes are nonuniform, particularly at low deformation time. This nonuniformity

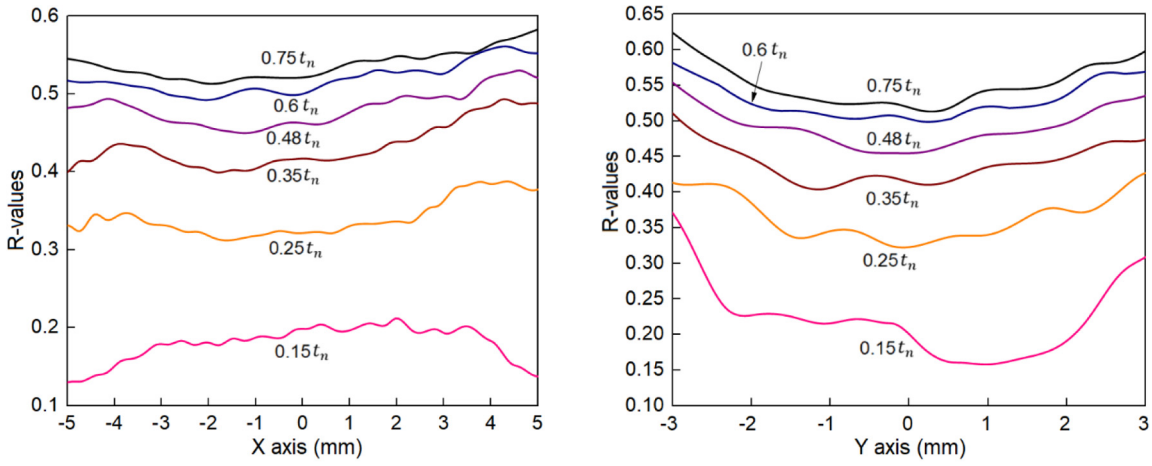

(a) r-value distribution along the X- and Y-axes for test condition I

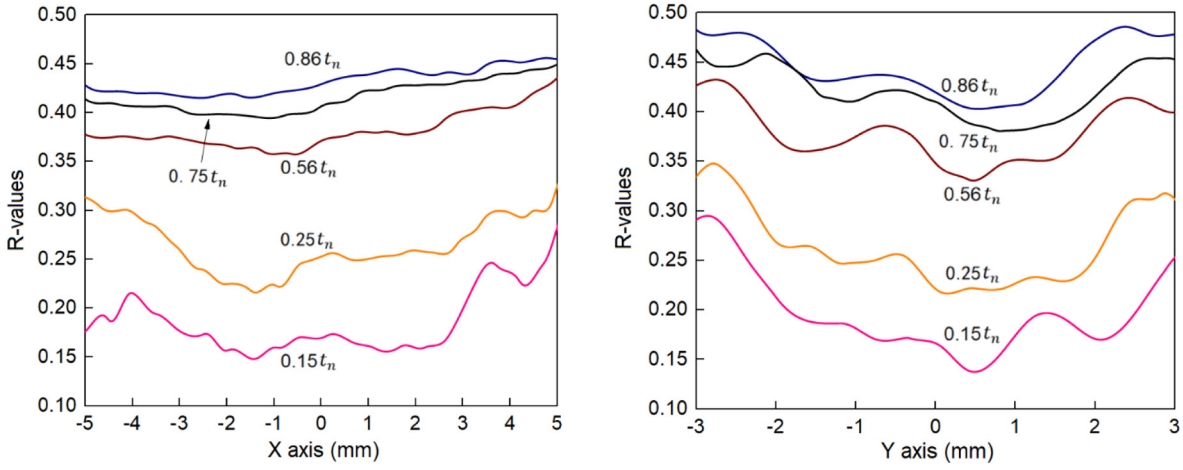

(b) r-value along the X- and Y-axes for test condition VI

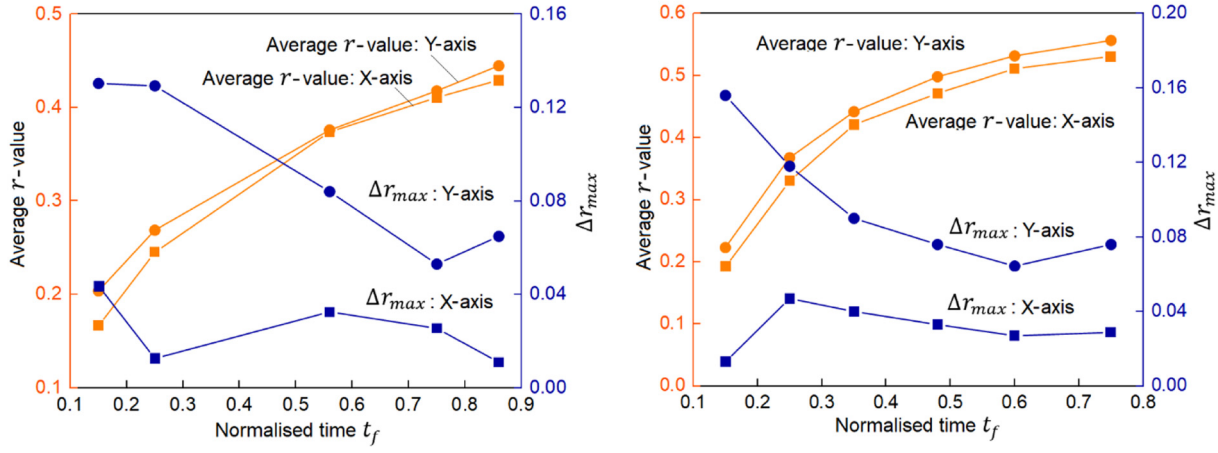

c) Average r-value and Δr_{max} evolution for I (d) Average r-value and Δr_{max} evolution for VI

Fig. 6. Evolutions of r-value distribution and Δr_{max} along the X- and Y-axes with increasing t_n for 500 °C and 0.1 s^{-1} (test condition I), and 350 °C and 0.5 s^{-1} (test condition VI).

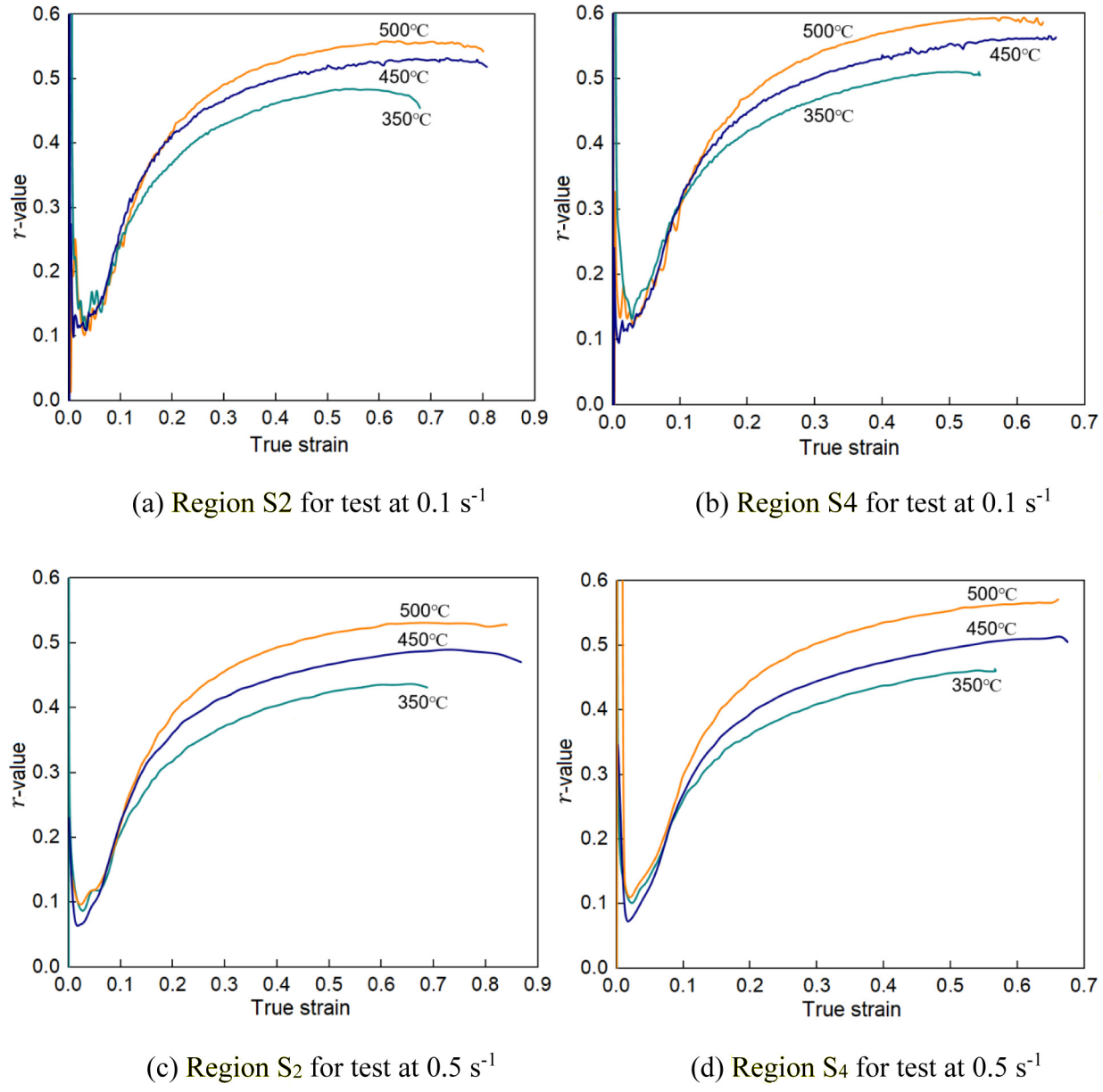

Fig. 7. Evolution of r-values across regions of S_2 and S_4 as a function of true strain (ε_x) for the Test Category I (strain rate of 0.1 s^{-1}) and Test Category II (strain rate of 0.5 s^{-1}).

of the r-value along both axes can be attributed to the temperature gradient along the gauge length of specimens [10].

To quantitatively compare the distribution of r-values and fluctuation evolution along the X- and Y-axes as deformation progresses, the average r-value was calculated within the range of −3 to 3 mm along both axes at different t_n as shown in Figures 6c and 6d. Additionally, the maximum r-value difference Δr_{max} along the X- and Y-axes is respectively calculated following the equation as:

$$\Delta r_{max} = r_{max} - r_{min} \tag{3}$$

where r_{max} and r_{min} respectively stand for the maximum and minimum r-values along the X- or Y-axes within the range from −3 to 3 mm at different t_n. It can be observed that the average r-value curves along the Y-axis for test conditions 1A and 2C is slightly higher than those along the X-axis during the deformation process at different t_n. Furthermore, the curves of average r-value for both specimens along the X- and Y-axes show a gradual increase at a decreasing rate with the proceeding of deformation. Additionally, Δr_{max} along the Y-axis for both specimens exhibit a higher value compared with that along the X-axis at different t_n, indicating that the r-value along the Y-axis has a higher extent of variation than that along the X-axis during deformation.

Figure 7 displays the evolution of the average r-value within regions S_2 and S_4 versus the major strain ε_x for specimens deformed at reference temperatures of 350 to 500 °C and strain rates of 0.1 and 0.5 s^{-1}. All the r-value curves demonstrate a trend of severely fluctuation at the

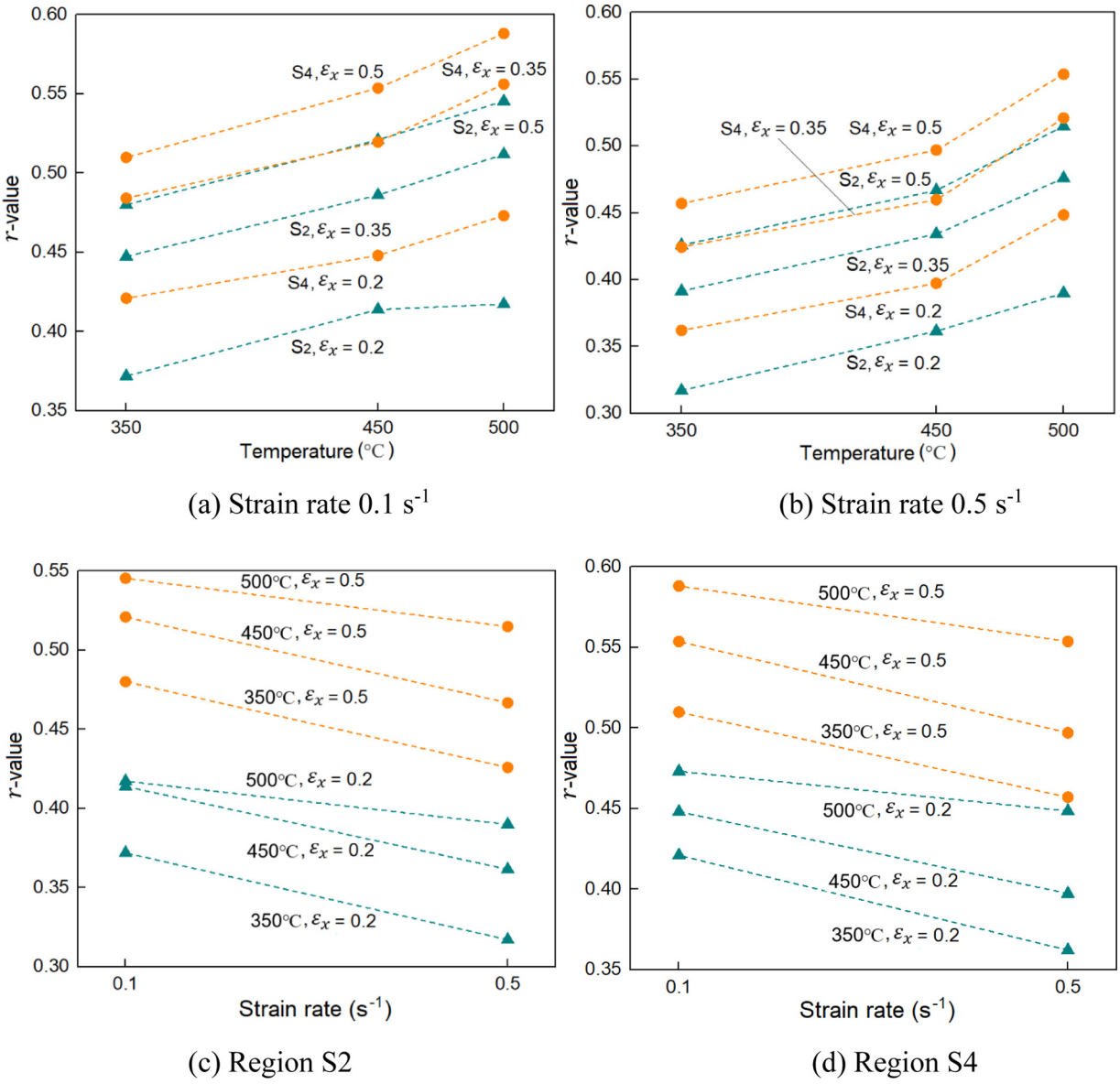

Fig. 8. Effect of deformation temperatures and strain rates on the evolutions of r-value within regions S_2 and S_4 with increasing major strain ε_x.

beginning of deformation. With the proceeding of deformation, the r-value curves exhibit an increasing trend at a decreasing rate until reaching their peak value in the latter stage during deformation. In addition, for each test conducted at the same strain rate and for the same region, the r-value increases with increasing temperature. Based on the definition of r-value, the increasing of r-value at various strain rates and temperatures indicates that the planar anisotropy reduces and the material becomes more isotropic as the deformation progresses.

Figure 8 exhibits the effects of various temperatures and strain rates on the evolution of r-value at increasing major strain ε_x. Specifically, Figures 8a and 8b demonstrates the r-value variations at reference temperatures of 350, 450, and 500 °C. It can be observed that when deformed at the same strain rate of 0.1 or 0.5 s^{-1}, increasing applied temperature increases the r-value obtained at the same major strain ($\varepsilon_x = 0.2, 0.35, 0.5$) and within the same area (S_2, S_4). In addition, a higher r-value is achieved with increasing area of the determining region (S_2, S_4) at the same major strain. Figures 8c and 8d exhibits the effect of strain rates on the r-value evolution. It can be noticed that the r-values obtained at 0.5 s^{-1} are lower than those at 0.1 s^{-1} when all other conditions (major strain, temperature, selected strain field) are the same. Furthermore, when comparing the r-values obtained at the same strain, strain rate, and applied temperature in different regions S_2 and S_4 as shown in Figure 8, the r-value in region S_2 is lower than that in region S_4.

Figure 9 presents the stress-strain curves determined from the DIC and C-gauge strain measurements at 500 °C and 0.1 s^{-1}. The curves determined using the measured strains within different regions (S_3, S_5, and S_6) and gauge lengths (L_3, L_5, and L_6) are demonstrated in Figure 9a.

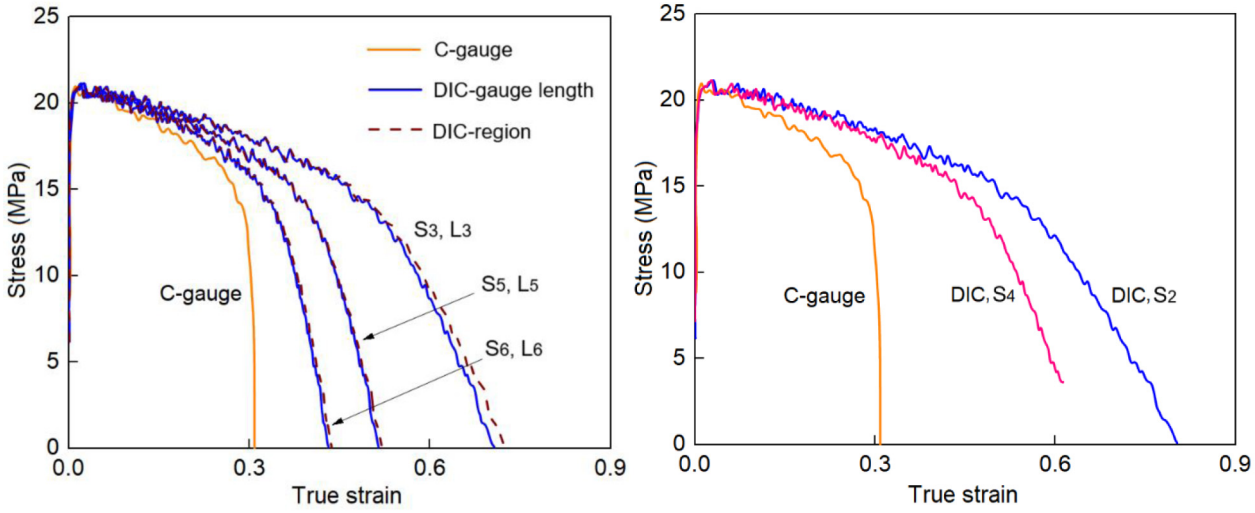

(a) Stress-strain curves for S_3, S_5 and S_6 (b) Stress-strain curves for S_2 and S_4

Fig. 9. True stress-strain curves determined from the measured strain data using C-gauge and DIC. The notations 'S_n' and 'L_n' where n is a number refer to the curves determined using respectively the n th DIC region and the gauge length having the same value as the length of the n th DIC region.

It should be noted that in the DIC measurement, the strain was measured using gauge lengths corresponding to the lengths of S_3, S_5, and S_6, which are labelled as L_3, L_5, and L_6 (equivalent to the lengths of 6, 12, and 16 mm) respectively. A notable difference can be observed between the stress-strain curves obtained from the DIC and C-gauge strain measurements. The stress for the C-gauge drops more significantly with increasing strain compared to the DIC, and the fracture strain for the C-gauge is much smaller than the DIC. Additionally, distinct variance in the evolution of the curves from different regions and gauge lengths are observed, with the fracture strain varying notably. However, minor discrepancies are observed between the curves of S_3 and L_3, S_5 and L_5, S_6 and L_6. This is attributed to the relatively uniform strain distributions along the specimen width direction as shown in Figure 5. Figure 9b shows two stress-strain curves determined from the strains measured within regions S_2 and S_4 respectively. Minor discrepancies are observed between these curves within the strain range of approximately 0 to 0.3. However, the discrepancies gradually increase when surpassing the strain around 0.3.

4 Discussion

4.1 Characteristics of the full field strain distribution

As observed in Figure 3c, a strong inhomogeneity of the temperature distribution exists along the length direction, with a temperature drop nearly 100 °C at the location of 15 mm away from the centre point O along the length direction. This inhomogeneity can be caused by heat loss to the specimen grip regions and the water cooling grips [10]. The higher temperature at the centre region of the specimen induces the strain localisation throughout both the early and later stages of the deformation as observed in Figure 4. This indicates that strain localisation observed in this study is dominated by heterogenous temperature distribution rather than other factors such as necking, particularly at the initial stages of deformation. Furthermore, the minor fluctuations in strain distribution along the width direction throughout the deformation process, as shown in Figure 4, indicate a more uniform temperature distribution along the width direction, which results in a minor effect of strain localisation in this direction.

Due to the inhomogeneity of the strain distribution along the gauge length, the selection of investigated regions or gauge lengths in the DIC measured strain fields exerts significant influence on the determination of the material's constitutive relationship. As demonstrated in Figure 9, the stress-strain curves determined from the Group I regions (S_2 and S_4) as well as the Group II regions (S_3, S_5, and S_6), exhibit various evolution trends after the initial stage of deformation and result in different fracture strains. Due to the strain localisation, the curves determined from the regions near the specimen centre, such as S_3 and S_2, exhibit the highest fracture strains, while those from the regions farther away, such as S_6 and S_4, show smaller fracture strains. Additionally, due to the high uniformity of distribution along the width direction, the curves determined using gauge length which equals to the region's length, such as S_6 and L_6, have minor differences as exhibited in Figure 9a.

4.2 Evolution patterns of planar anisotropy

With the increase of ε_x and ε_y, the r-values as exhibited in Figures 4 and7, demonstrate an increasing trend with the proceeding of deformation. Based on the definition of r-value, this increasing trend indicates that the planar anisotropy reduces and the material becomes more isotropic as the deformation progresses.

The r-value is strongly location dependent that its value at various locations can vary distinctly as manifested in Figure 4. When comparing at different locations as shown in Figure 4b, the r-values at points 4 and 5 are higher than the value at point 6 within region S_4. Additionally, for the points within S_2, the r-values at 1 and 2 are higher than 3. The r-values at these selected points indicate a trend of decreasing anisotropy at locations with larger distance to the centre line along the length direction (X-axis) during deformation. Furthermore, when comparing the average r-values within the regions from S_1 to S_4, the r-value increases with the expanding of area from S_1 to S_4. This increase of r-value as the region expands from the origin point O manifests higher anisotropy in the nearer areas surrounding point O during deformation. On the other hand, for the average r-values within the regions of S_3, S_5, and S_6 having the same width of 6 mm but different lengths from 6 to 15 mm, no distinct difference is exhibited in the r-values among these three regions as shown in Figure 4d. Thus, the variation in r-value is more sensitive to location/area changes along the Y-axis direction compared to the X-axis for the specimen, which is consistent with the observation that Δr_{max} along the Y-axis is larger than along the X-axis during deformation as exhibited in Figures 6c and 6d. As a result, although the temperature gradient is more sensitive in the length direction than in the width direction, the r-value is more affected by location changes along the width direction.

4.3 Effects of temperature and strain rate on planar anisotropy

The dependence of the alloy's planar anisotropy on deformation temperature and strain rate during deformation has been previously reported [29,30]. In this study, this dependence has also been identified, as shown in Figure 8. For the effects of various temperatures on the observed planar anisotropy (Figs. 8a to 8b), the r-value increases as the temperature rises from 350 to 500 °C when compared at the same strain ε_x (0.2, 0.35, 0.5), same regions (S_2, S_4), and same strain rate (0.1 s^{-1}, 0.5 s^{-1}). This indicates that for the AA6082 investigated in this study, its planar anisotropy decreases with increasing temperature. A similar trend has been reported for AA6016 in [31]. Increasing temperature can lower the activation energy for dislocation motion and prompt the activation of crystallographic slip systems [32,33]. Consequently, it can reduce the differences in the resistance to deformation at various directions and induce lower planar anisotropy [31]. Regarding the effect of strain rate on the planar anisotropy, Figures 8c–8d demonstrate that the r-value of AA6082 decreases when the strain rate increases from 0.1 to 0.5 s^{-1}, while keeping other conditions (temperature, selected strain fields, major true strain) constant. This indicates a promotion in planar anisotropy of AA6082 with increasing strain rate during deformation.

4.4 Comparison of different strain measurements through proposed empirical equation

From the discussion in Sections 4.2 and 4.3, it is clear that the planar anisotropy of AA6082 varies not only with the proceeding of deformation, but also highly depends on the deformation temperature and strain rate. To model the r-value evolution versus strain, a novel empirical equation is formulated in the present study as follows:

Table 3. Material constants for r-value evolution with increasing ε_x of AA6082.

A_1 for S_2	A_1 for S_4	B_1	n_1	n_2 for S_2
190	204	5.66	8.4	2.52E-2
n_2 for S_4	Q(J/mol)	R(J/(mol·k))	$\dot{\varepsilon}_r(s^{-1})$	
2.82E-2	4800	8.314	1	

$$\begin{cases} \dot{r} = A/(B(\tanh(\varepsilon_x)+1)^{n_1}) \\ A = A_1 \exp\left(-\dfrac{Q}{RT}\right) \\ B = B_1\left(\dot{\varepsilon}_x/\dot{\varepsilon}_r\right)^{n_2} \end{cases} \tag{4}$$

where $\dot{r}$ represents the changing rate of the r-value. In the equation. A and B are employed as temperature- and strain rate-dependent parameters, respectively, to capture their effects on r-value evolution. The parameter A is formulated using the classical Arrhenius equation that is used to express the effect of temperature; Q, R, and T denote the activation energy, gas constant, and absolute temperature, respectively. The parameter B is directly related to the strain rate $\dot{\varepsilon}_x$. $\dot{\varepsilon}_r$ stands for the referenced strain rate equals to 1 s^{-1}. It should be noted that both A and B are unitless. A_1, B_1, n_1, and n_2 are material constants. The material constants employed for predicting r-value evolution within regions S_2 and S_4 are listed in Table 3 . It should be noted that A_1 and n_2 were determined for regions S_2 and S_4, separately.

Figure 10 shows the predicted r-values derived from the proposed empirical equations and their comparison with the experimental r-values determined from regions S_2 and S_4 using DIC measurements. The results exhibit a good agreement between the predicted and experimental results of r-value evolution as the strain increases. Additionally, the evolution of the r-value obtained from different regions can be differentiated by adopting different values for A_1 and n_2. As a result, the constructed empirical equation is capably of modelling the variations in r-value evolution when deformed at different temperatures and strain rates within different regions of S_2 and S_4. The empirical equation for the r-value proposed in this study will benefit for both experimental investigations and modelling of metallic materials under hot stamping conditions. In particular, the equation enables the determination of longitudinal strain considering for anisotropy between the specimen's length and width directions during deformation within specific temperature and strain rate range in the hot stamping state. Furthermore, it can be incorporated into numerical simulations to more accurately predict the full-field plane strain behaviour during deformation. In addition, it should be noted that in this study the evolution of r-value during the uniaxial tensile process was investigated using DIC measurements for AA6082. For other aluminium alloys or materials (such as steel or titanium), the material constants required to capture the r-value can be

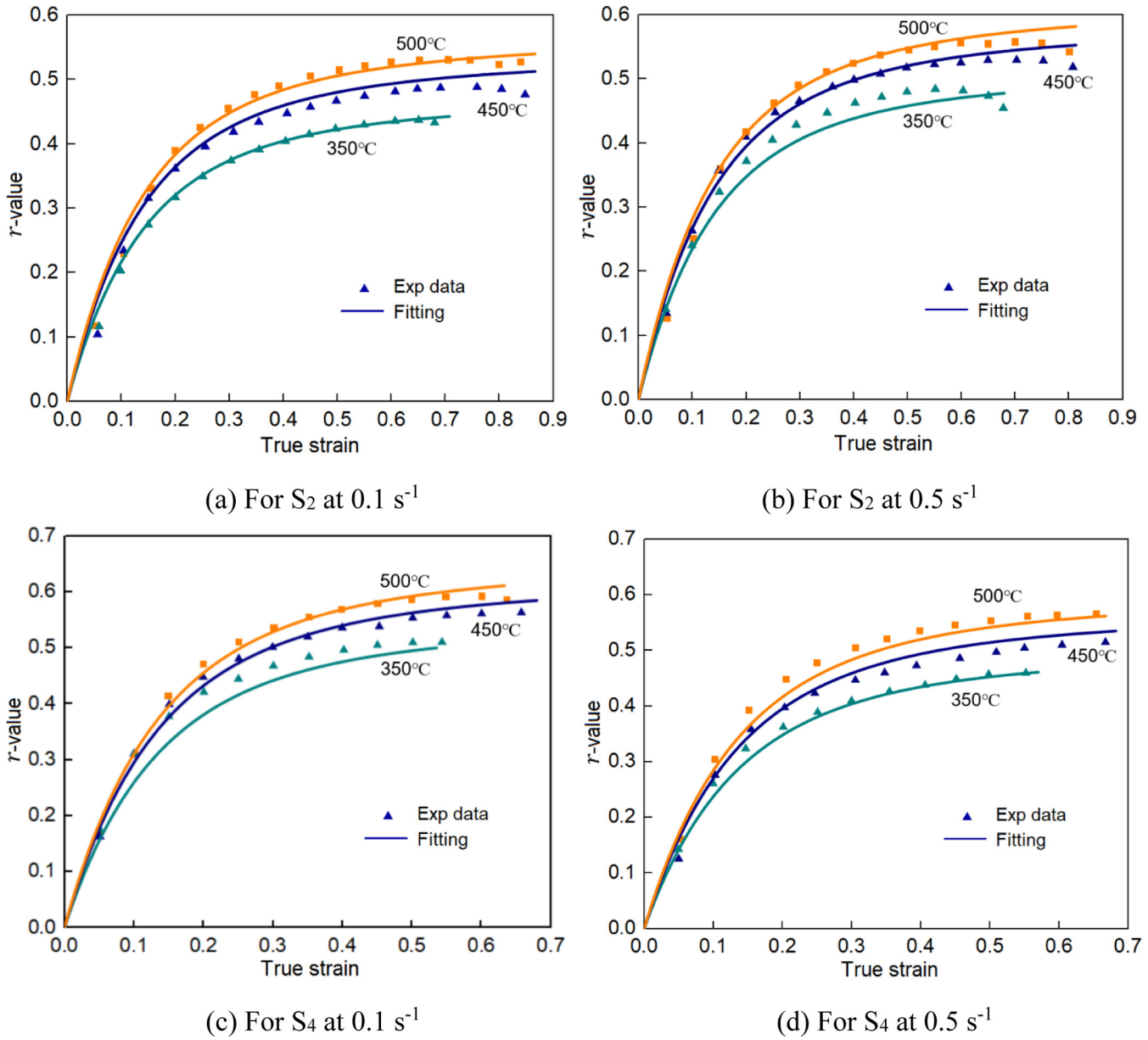

Fig. 10. Fitting results (solid lines) of r-value evolutions with increasing ε_x for S_2 and S_4 at strain rate of 0.1 and 0.5 s^{-1}. The symbols stand for the experimental data.

different, however, these constants in the empirical equations can be determined from experimental data obtained using the same method provided in this study. Based on the determined r-value evolutions in the uniaxial process, the interrelation between the material deformation behaviour measured using the C-gauge and DIC methods can be further revealed, as illustrated in the following context.

In this study, both C-gauge and DIC methods were employed to measure the strain for AA6082 sheets deformed at 500 °C and 0.1 s^{-1} and it is found that the two methods have a significant effect on obtained stress-strain curve during hot deformation (see Fig. 9). However, it should be noted that the C-gauge strain measurements assume $\varepsilon_x = -2\varepsilon_y$, which neglects the planar anisotropy of the alloy. To account for the planar anisotropy, the relation obtained from equation (2) as $\varepsilon_x = -\varepsilon_y(1/r+1)$ was employed to correct the stress-strain relation determined from C-gauge. In this equation, ε_y represents the strain measured by the C-gauge, r is the corresponding r-values. Therefore, by employing the experimentally determined r-values in Figures 7a and 7b, and predicted r-values in Figures 10a and 10c, two corrected stress-strain curves were obtained.

Figure 11 further illustrates the comparison between the material deformation behaviour measured by the C-gauge and DIC, as well as the corrected results using the r-value derived from the empirical equation. Figures 11a and 11b show the two corrected true stress-strain curves labelled as experiment-corrected (Exp-corr) and prediction-corrected (Pred-corr), as well as the original curves obtained from the measured strains using C-gauge and DIC methods, respectively for regions S_2 and S_4. As

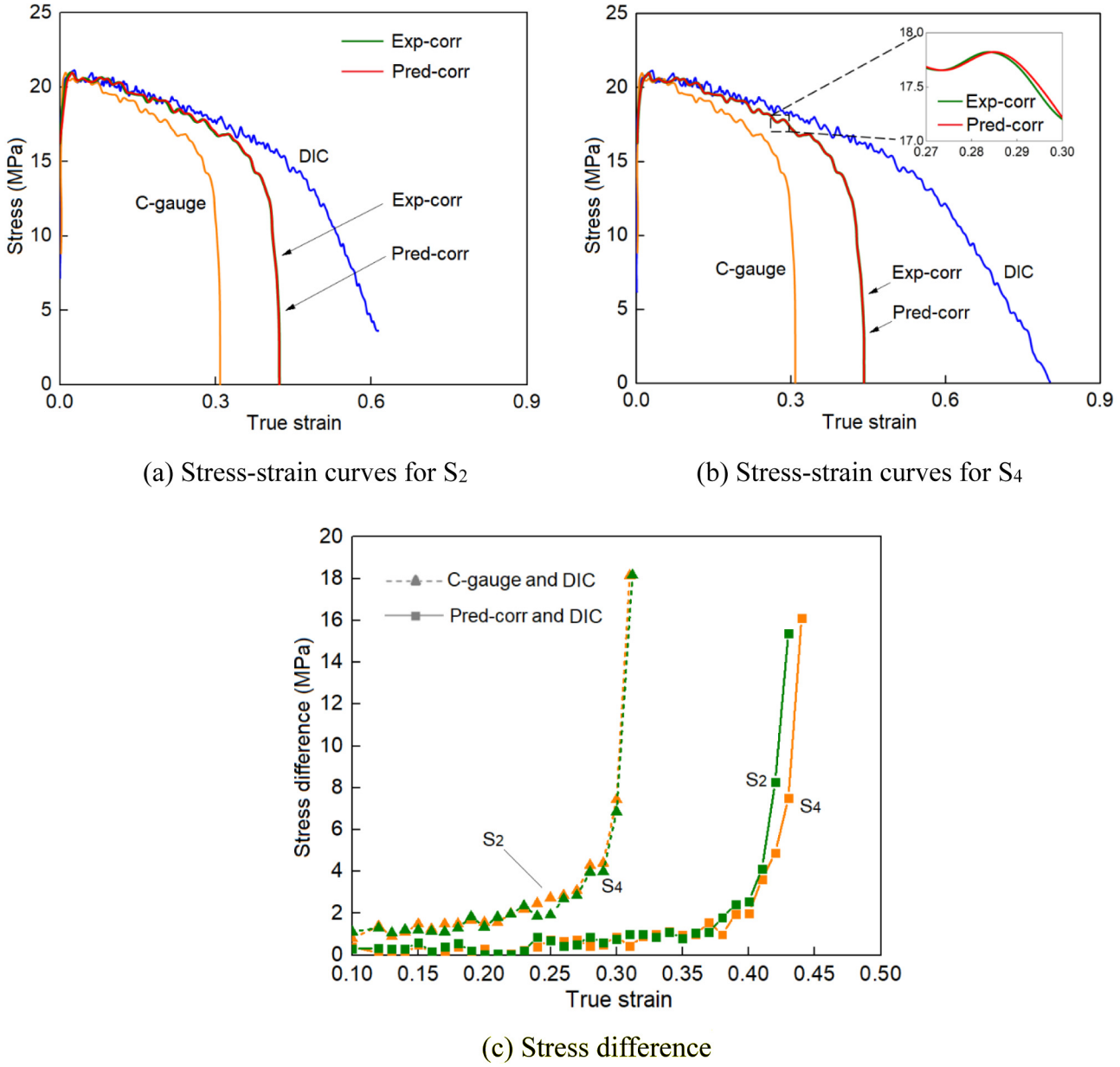

Fig. 11. Stress-strain curves obtained using strains measured via C-gauge and DIC and using C-gauge strains corrected using the experimental r-value (Exp-corr) and predicted r-value (Pred-corr), for the test condition at 500 °C and 0.1 s^{-1}, as well as the stress difference compared to the DIC curves at the same strain. S_2 and S_4 in (c) denote the regions for measurement.

shown in Figures 11a and 11b, there is little difference between the Exp-corr and Pred-corr curves, indicating that the prediction of r-values from equation (4) is satisfactory. As observed in Figures 11a and 11b, good agreement is achieved among all the curves during the initial stage of deformation. However, as deformation progresses, the differences between the curves gradually increase, especially for the C-gauge curves compared to others. In addition, Figure 11c shows the stress differences between the Pred-corr and DIC curves, as well as between the C-gauge and DIC curves, plotted as a function of the true strain up to the fracture points of the Pred-corr and C-gauge curves respectively. As demonstrated in the figure, the stress differences of C-gauge to DIC are significantly larger than the differences of the Pred-corr to DIC, while only minor differences are identified between the curves determined within regions S_2 and S_4 for C-gauge and DIC, as well as Pred-corr and DIC respectively. When comparing the stress difference at the strain of 0.25, the maximum difference of C-gauge to DIC is 14.3%, while the difference of Pred-corr to DIC is 3.8%. The C-gauge curve is obtained by transforming the measured strain in the specimen width direction (ε_y) to the length direction strain (ε_x) under the assumption of planar isotropy ($r = 1$) as illustrated in equation (2). As a result, the pronounced difference in the C-gauge curves can be attributed to this

isotropy assumption, while neglecting anisotropy—particularly between the width and length directions during deformation—leads to noticeable discrepancies when compared with the DIC results. On the other hand, this highlights the improved measurement accuracy achieved by adopting the r-value correction to consider the effect of planar anisotropy.

5 Conclusions

In this study, the planar anisotropy of AA6082 sheets and its evolution during uniaxial tensile deformation at temperatures ranging from 350 to 500 °C and strain rates of 0.1 and 0.5 s^{-1} have been investigated. The DIC strain measurement method has been adopted to obtain the distribution and evolution patterns of the r-value (also known as the Lankford coefficient) with proceeding of deformation, as well as to analyse the effects of applied temperature and strain rate on the r-value. An empirical equation to model r-value evolution with progression of deformation has been constructed and verified with experimental data under different conditions. The true stress-strain relations obtained from C-gauge and DIC strain measurements, as well as the corrected stress-strain relation using the r-value are compared. The main conclusions can be summarised as follows:

- The r-value of AA6082 depends on deformation level. It evolves with deformation in a similar trend under different testing conditions. Specifically, it starts at a low value of approximately 0.1 and increases at a decreasing rate, until reaching a peak value of approximately 0.5 at the end of deformation.
- The r-value of AA6082 depends on both deformation temperature and strain rate. The r-value increases as temperature rises, with a maximum increase of 23% when deformed from 350 to 500 °C at 0.1 or 0.5 s^{-1}. Conversely, the r-value decreases as strain rate increases, with a maximum reduction of 12% from 0.5 to 0.1 s^{-1} at 450 °C.
- The proposed empirical equation for modelling r-value evolution incorporates temperature- and strain rate-dependent parameters. It effectively captures the effects of varying temperatures and strain rates on r-value evolution of AA6082, as evidenced by satisfactory agreements with the experimental data.
- A significant distinction is observed between the stress-strain curves obtained using the C-gauge and DIC strain measurement methods for AA6082, with an absolute stress difference of 14.3% relative to the DIC at the strain of 0.25.

Funding

This work was supported by the Engineering and Physical Sciences Research Council (EPSRC) [Grant number EP/R001715/1] on "Lightform: Embedding Materials Engineering in Manufacturing with Light Alloys.

Conflicts of interest

The authors declare that they have no known competing financial interests or personal relationships that could have appeared to influence the work reported in this paper.

Data availability statement

The data that support the findings of this study are available from the corresponding author upon reasonable request.

Author contribution statement

Xi Wang: Methodology, Investigation, Formal analysis, Writing - Original Draft. Ruiqiang Zhang: Methodology, Formal analysis, Supervision, Writing - Review & Editing. Zhusheng Shi: Writing - Review & Editing. Jianguo Lin: Conceptualization, Funding acquisition, Writing - Review & Editing.

References

1. T. Taylor, Critical review of automotive hot-stamped sheet steel from an industrial perspective, Mater. Sci. Technol. **34** (2018) 809–861
2. T. Maeno, K. Mori, R. Yachi, Hot stamping of high-strength aluminium alloy aircraft parts using quick heating, CIRP Annals. **66** (2017) 269–272
3. H. Karbasian, A. Tekkaya, A review on hot stamping, J. Mater. Process. Technol. **210** (2010) 2103–2118
4. G. Atxaga, A. Arroyo, B. Canflanca, Hot stamping of aerospace aluminium alloys: automotive technologies for the aeronautics industry, J. Manuf. Process. **81** (2022) 817–827
5. J. Lv, J. Yu, Z. Shi, W. Li, J. Lin, Feasibility study of a novel multi-container extrusion method for manufacturing wide aluminium profiles with low force, J. Manuf. Process. **85** (2023) 584–593
6. Y. Li, Y. Zhang, S. Li, Viscoplastic constitutive modeling of boron steel under large strain conditions and its application in hot semi-cutting, J. Manuf. Process. **66** (2021) 532–548
7. H. Xiao, X. Fan, M. Zhan, B. Liu, Z. Zhang, Flow stress correction for hot compression of titanium alloys considering temperature gradient induced heterogeneous deformation, J. Mater. Process. Technol. **288** (2021) 116868
8. S. Jiang, Z. Zhang, Z. Shi, J. Lin, Unravelling dynamic recrystallisation behaviour in AA7050 under hot forging conditions, Mater. Charact. **211** (2024) 113887
9. H. Li, L. He, G. Zhao, L. Zhang, Constitutive relationships of hot stamping boron steel B1500HS based on the modified Arrhenius and Johnson-Cook model, Mater. Sci. Eng.: A. **580** (2013) 330–348
10. R. Zhang, J. Jiang, J. Lin, V. Yardley, Investigation of variability in apparent values of materials properties in thermo-mechanical uniaxial tensile tests on sheet metals, J. Manuf. Process. **101** (2023) 737–754
11. Y. Li, S. Li, Y. Chen, G. Han, Constitutive parameters identification based on DIC assisted thermo-mechanical tensile test for hot stamping of boron steel, J. Mater. Process. Technol. **271** (2019) 429–443

12. J. Rakhmonov, M. Qassem, D. Larouche, K. Liu, M. Josée, J. Colbert et al., A new approach to determine tensile stress-strain evolution in semi-solid state at near-solidus temperature of aluminum alloys. Metals. **11** (2021) 1–13.
13. A. Phillion, S. Thompson, S. Cockcroft, M. Wells, Tensile properties of as-cast aluminum alloys AA3104, AA6111 and CA31218 at above solidus temperatures, Mater. Sci. Eng.: A. **497** (2008) 388–394
14. T. Baross, P. Bereczki, L. Jánosi, G. Veres, The bonded area growth at diffusion bonding determined by the numerical modelling of Gleeble 3800 experiments and in comparison with the model by Hill and Wallach, Fusion Eng. Des. **194** (2023) 113707
15. A. Bolouri, K. Liu, X. Chen, Effects of iron-rich intermetallics and grain structure on semisolid tensile properties of Al-Cu 206 cast alloys near solidus temperature, Metall. Mater. Trans. A. **47** (2016) 6466–6480
16. A. Nikki, K. Prakriti, K. Vinod, K. Nilesh, A. Ramkishor, D. Sourav, Simulated stress induced sensitization of HAZ in multipass weld of 304LN austenitic stainless steel, J. Manuf. Process. **62** (2021) 784–796
17. C. Bennett, S. Leen, E. Williams, P. Shipway, T. Hyde, A critical analysis of plastic flow behaviour in axisymmetric isothermal and Gleeble compression testing, Comput. Mater. Sci. **50** (2010) 125–137
18. A. Phillion, S. Cockcroft, P. Lee, A new methodology for measurement of semi-solid constitutive behavior and its application to examination of as-cast porosity and hot tearing in aluminum alloys, Mater. Sci. Eng.: A. **491** (2008) 237–247
19. A. Mishchenko, A. Scotti, Welding thermal stress diagrams as a means of assessing material proneness to residual stresses, J. Mater. Sci. **56** (2021) 1694–1712
20. M. Ganapathy, N. Li, J. Lin, M. Abspoel, D. Bhattacharjee, A novel grip design for high-accuracy thermo-mechanical tensile testing of boron steel under hot stamping conditions, Exp. Mech. **58** (2018) 243–258
21. N. Li, C. Sun, N. Guo, M. Mohamed, J. Lin, T. Matsumoto et al., Experimental investigation of boron steel at hot stamping conditions, J. Mater. Process. Technol. **228** (2016) 2–10
22. J. Zhou, B. Wang, M. Huang, Two constitutive descriptions of boron steel 22MnB5 at high temperature, Mater. Des. **63** (2014) 738–748
23. H. Wang, P. Ge, S. Wu, B. Wang, Y. Wang, X. Kong et al., Improvement method of high-temperature digital image correlation measurement accuracy based on image processing, Measurement. **190** (2022) 110723
24. Y. Wang, W. Zhang, H. Huang, W. Zhong, Chen, F. Zhili, Clarification of creep deformation mechanism in heat-affected zone of 9Cr steels with In Situ experiments, Scripta Mater. **194** (2021) 113640
25. Z. Shao, N. Li, J. Lin, T. Dean, Development of a new biaxial testing system for generating forming limit diagrams for sheet metals under hot stamping conditions, Exp. Mech. **56** (2016) 1489–1500
26. S. Chen, R. Zhang, Z. Shi, J. Lin, An improved DIC method for full-field strain measurement in tensile tests on aluminium alloys under hot stamping conditions, Int. J. Lightweight Mater. Manuf. **7** (2024) 438–449
27. R. Zhang, Z. Shao, J. Lin, T. Dean, Measurement and analysis of heterogeneous strain fields in uniaxial tensile tests for boron steel under hot stamping conditions, Exp. Mech. **60** (2020) 1289–300
28. Y. Li, S. Li, Y. Chen, G. Han, Constitutive parameters identification based on DIC assisted thermo-mechanical tensile test for hot stamping of boron steel, J. Mater. Process. Technol. **271** (2019) 429–443
29. J. Huh, H. Huh, C. Lee, Effect of strain rate on plastic anisotropy of advanced high strength steel sheets, Int. J. Plast. **44** (2013) 23–46
30. F. Shen, S. Münstermann, J. Lian, An evolving plasticity model considering anisotropy, thermal softening and dynamic strain aging, Int. J. Plast. **132** (2020) 102747
31. S. Kurukuri, A. Miroux, M. Ghosh, A. Boogaard, Effect of temperature on anisotropy in forming simulation of aluminum alloys, Int. J. Mater. Forming. **2** (2009) 387–390
32. D. Pagan, J. Bernier, D. Dale, J. Peter, T. Turner, B. Blank et al., Measuring Ti-7Al slip system strengths at elevated temperature using high-energy X-ray diffraction, Scripta Mater. **142** (2018) 96–100
33. B. Zhao, P. Huang, L. Zhang, S. Li, Z. Zhang, Q. Yu, Temperature effect on stacking fault energy and deformation mechanisms in titanium and titanium-aluminium alloy, Sci. Rep. **10** (2020) 3086

Cite this article as: Xi Wang, Ruiqiang Zhang, Zhusheng Shi, Jianguo Lin, Investigation of planar anisotropy evolution in aluminium alloy sheets under hot stamping conditions using digital image correlation, Manufacturing Rev. **12**, 22 (2025), https://doi.org/10.1051/mfreview/2025017